

# Spontaneous water dissociation on intermetallic electride $\text{LaCu}_{0.67}\text{Si}_{1.33}$ enhances electrochemical methanization of $\text{CO}_2$

Received: 4 September 2024

Accepted: 21 May 2025

Published online: 30 May 2025



Luming Zhang<sup>1,2,3,7</sup>, Huan Ma<sup>2,4,5,7</sup>, Yongfang Sun<sup>4,7</sup>, Yilin Zhao<sup>3</sup>, Huiying Deng<sup>6</sup>, Yuhang Wang<sup>6</sup>, Fei Wang<sup>4</sup>✉, Xiao-Dong Wen<sup>1,2,4,5</sup>✉ & Mingchuan Luo<sup>3</sup>✉

Renewable electricity driven  $\text{CO}_2$  electroreduction into methane offers a sustainable route to mitigate our dependence on natural gas. However, this route is now limited by the unsatisfied efficiency and short durability, which originates from a kinetic disparity between water dissociation (WD) and proton-coupled electron transfer on existing catalysts. Herein, we harness the exceptional WD capability of the intermetallic electride (IE) materials for the electrocatalytic methanization from  $\text{CO}_2$ . Combinative experimental and theoretical approaches strongly evidence a spontaneous WD on an IE  $\text{LaCu}_{0.67}\text{Si}_{1.33}$  catalyst due to its unique electronic structure (strongly modified charge states, reversible lattice hydride ions and anionic electrons). Consequently, this catalyst exhibits improved methanization performance in alkaline flow cells, achieving a methane Faraday efficiency of 72% at  $-1.21\text{ V}$  versus the reversible hydrogen electrode (vs. RHE) and peak partial current density of  $476.7\text{ mA cm}^{-2}$  at  $-1.52\text{ V}$  vs. RHE. Energetic calculations further establish the mechanistic link between WD and methanization processes on our catalyst, on which a lowered free energy barrier for the key  $^*\text{CO}$  to  $^*\text{CHO}$  transformation step is observed. This work sheds light on the pivotal role of WD and expands the repertoire of materials for efficient electrocatalytic methanization from  $\text{CO}_2$ .

The renewable-electricity-powered electrochemical  $\text{CO}_2$  reduction ( $\text{CO}_2\text{RR}$ ) to methane is an appealing pathway to regenerate natural gas from carbon emissions<sup>1–3</sup>. Aiming to industrializing this pathway, vast efforts have been devoted to designing more efficient Cu-based catalysts with improved activity, selectivity, and stability<sup>4–7</sup>. Such catalyst

design was mainly guided by the classic descriptor-based approach, in which the outcome of a catalyst is depicted by its binding strengths to carbonaceous intermediates. For  $\text{CO}_2\text{RR}$ , the binding energy of adsorbed carbon monoxide ( $\text{CO}_{\text{ad}}$ ) serves as a common and simple descriptor due to the universal scaling relation among all

<sup>1</sup>College of Chemistry and Chemical Engineering, Taiyuan University of Technology, Taiyuan, P. R. China. <sup>2</sup>National Energy Center for Coal to Liquids, Synfuels China Co., Ltd, Huairou District, Beijing, P. R. China. <sup>3</sup>School of Materials Science and Engineering, Peking University, Beijing, China. <sup>4</sup>State Key Laboratory of Coal Conversion, Institute of Coal Chemistry, Chinese Academy of Sciences, Taiyuan, P. R. China. <sup>5</sup>University of Chinese Academy of Sciences, No. 19A Yuquan Road, Beijing, P. R. China. <sup>6</sup>Institute of Functional Nano & Soft Materials (FUNSOM), Soochow University, 199 Ren'ai Road, Suzhou, Jiangsu, China.

<sup>7</sup>These authors contributed equally: Luming Zhang, Huan Ma, Yongfang Sun. ✉ e-mail: [wangfei908@sxicc.ac.cn](mailto:wangfei908@sxicc.ac.cn); [wxd@sxicc.ac.cn](mailto:wxd@sxicc.ac.cn); [m.luo@pku.edu.cn](mailto:m.luo@pku.edu.cn)

carbonaceous species<sup>8,9</sup>. Nevertheless, recent findings unravel other factors, in addition to carbonaceous adsorption, also depict the electrochemical methanization from CO<sub>2</sub><sup>10–14</sup>. In particular, promoting WD on a catalyst enhances the methanization because (1) CO<sub>2</sub>RR necessitates molecular water as hydrogen source<sup>15</sup>, (2) methane is a deeply hydrogenated product and involves the transfer of eight electrons and six hydrogens<sup>16</sup>, (3) The hydrogenation of CO<sub>ad</sub> to CH<sub>x</sub>O<sub>ad</sub> (x = 1, 2, 3) is widely recognized as the rate-determining step along the methanization pathway<sup>17,18</sup>.

Established knowledge from the alkaline water electrocatalysis indicates the hydroxyl-favoring materials, e.g., metal hydroxide or oxides, could promote the rate of WD in alkaline/neutral environments<sup>19,20</sup>. Levering this knowledge, previous studies have designed electrocatalytic interfaces between CO<sub>2</sub>-active Cu-based components and hydroxyl-favoring components for CO<sub>2</sub>RR. Indeed, a positive link between the electrosynthesis of methane and WD was found and rationalized<sup>21</sup>. Though the effectiveness of these heterojunction approaches for methanization, the intrinsically multiphase catalysts encountered challenge of structural stability and thus performance sustainability during CO<sub>2</sub>RR<sup>22–25</sup>. In particular, metal hydroxides or oxides are apt to be reduced under negative bias and the co-presence of H<sub>2</sub> (byproduct from CO<sub>2</sub>RR). This then desires a single-phase metallic alternative to the aforementioned multiphase catalysts for synchronizing WD and CO<sub>2</sub> activation. Recently, on an emerging class of IE materials, we observed spontaneous WD when studying water-induced structural evolution<sup>26,27</sup>. Distinct from conventional alloys, IEs consist of transition metals with strongly modified charge states, reversible lattice hydride ions and anionic electrons, which facilitate the dissociation of small molecules,

including H<sub>2</sub>O<sup>27</sup>, N<sub>2</sub><sup>28</sup> and CO<sub>2</sub><sup>29</sup> et al. This inspired us to design IE-based catalysts with balanced WD and CO<sub>2</sub> activation.

In this work, we applied IE-based nanomaterials for CO<sub>2</sub>RR and reported a class of IE LaCu<sub>0.67</sub>Si<sub>1.33</sub> catalyst for the electrochemical methanization. After verifying the structural features of IE using various characterizations, we systematically probed the WD behaviors of this IE catalyst using H<sub>2</sub>O-temperature-programmed surface reaction and energetic calculations, which confirmed a spontaneous WD on this IE surface. When tested in an alkaline flow cell, the IE LaCu<sub>0.67</sub>Si<sub>1.33</sub> catalyst showed a methane Faradaic efficiency (FE) of 72% at a reduction potential of −1.21 V vs. RHE, along with a partial current density of 476.7 mA cm<sup>−2</sup> at −1.52 V vs. RHE. In situ Fourier transform infrared spectroscopy observed that, compared to the Cu control, the IE LaCu<sub>0.67</sub>Si<sub>1.33</sub> catalyst showed a strengthened atop-adsorbed CO and a lowered ratio of free and weakly hydrogen-bonded water. DFT calculations further showed the methanization pathway to be energetically more favorable on the IE LaCu<sub>0.67</sub>Si<sub>1.33</sub> catalyst.

## Results

### Synthesis and characterizations of IE LaCu<sub>0.67</sub>Si<sub>1.33</sub>

We synthesized IE LaCu<sub>0.67</sub>Si<sub>1.33</sub> catalysts using a sequential methodology that encompasses electric arc-melting followed by high-energy ball milling, which yields nanoparticles in size of hundreds of nanometers (Supplementary Figs. 1, 2). The X-ray diffraction (XRD) patterns of as-synthesized materials exhibit an alignment of diffraction peaks with the standard card of ICSD#103038 (Fig. 1a), signifying our successful synthesis of IE LaCu<sub>0.67</sub>Si<sub>1.33</sub> with a hexagonal phase (adhering to the AlB<sub>2</sub> structure, p6/mmm space group)<sup>30,31</sup>. Lattice fringes can be clearly visualized from the high-resolution transmission electron microscopy (HRTEM) image of IE LaCu<sub>0.67</sub>Si<sub>1.33</sub>, affirming its

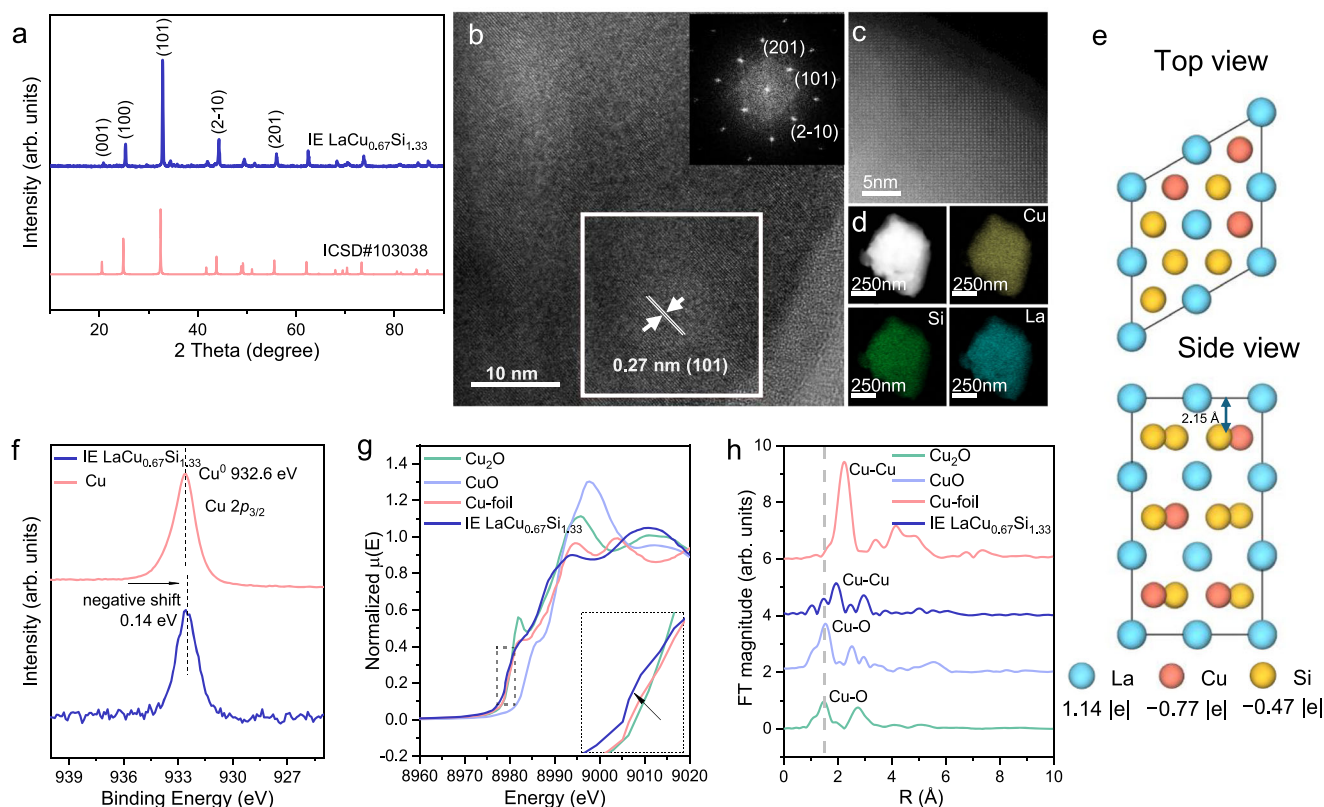


**Fig. 1 | Structural characterizations of the IE LaCu<sub>0.67</sub>Si<sub>1.33</sub> catalyst.** **a** XRD patterns. **b** HRTEM image and the corresponding FFT patterns (inset) and **c** High-resolution HAADF-STEM image. **d** The corresponding EDS elemental mapping for La, Cu, and Si. **e** Unit cell structure of IE LaCu<sub>0.67</sub>Si<sub>1.33</sub> (top and side

views) along with the results of Bader charge analysis. **f** High-resolution Cu 2p XPS profiles of IE LaCu<sub>0.67</sub>Si<sub>1.33</sub> and Cu samples. **g** XANES and **h** EXAFS spectra of Cu K-edge for Cu<sub>2</sub>O, CuO, Cu foil and IE LaCu<sub>0.67</sub>Si<sub>1.33</sub>. Source data are provided as a Source Data file.

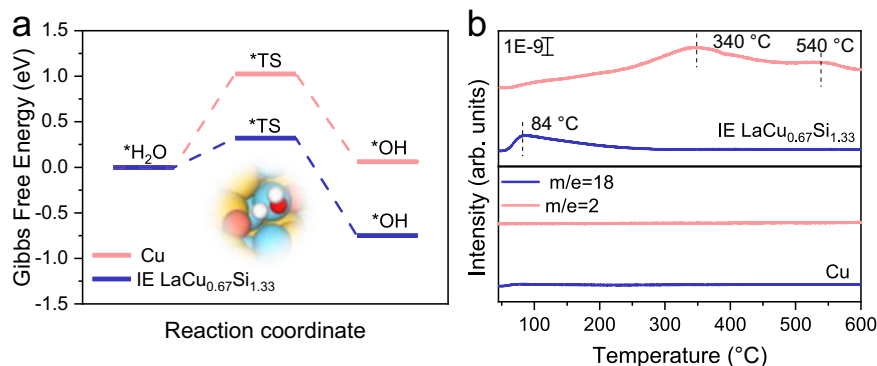


**Fig. 2 | Analysis of WD. a** Gibbs free energy diagram for H<sub>2</sub>O dissociation on IE LaCu<sub>0.67</sub>Si<sub>1.33</sub>(101) and Cu(111) surfaces. **b** Mass signals of H<sub>2</sub>O-TPSR over the IE LaCu<sub>0.67</sub>Si<sub>1.33</sub> catalyst and Cu control. The signal of *m/e* = 18 is H<sub>2</sub>O, and of *m/e* = 2 is H<sub>2</sub>. Source data are provided as a Source Data file.

crystallinity nature (Fig. 1b). A selected-area electron diffraction pattern (inset) confirms the presence of the respective (101), (201), (2–10) plane of IE LaCu<sub>0.67</sub>Si<sub>1.33</sub>, which aligns perfectly with the XRD results. High angle annular dark field-scanning transmission electron microscopy (HAADF-STEM, Fig. 1c) image further provides intricate details on the atomic arrangement, while the accompanying energy-dispersive X-ray spectroscopy (EDX) elemental mappings illustrate the uniform distribution of La, Cu, and Si throughout the entire crystal domain (Fig. 1d and Supplementary Fig. 3).

The unit cell of IE LaCu<sub>0.67</sub>Si<sub>1.33</sub> was meticulously constructed using density functional theory (DFT) calculations, synergistically enhanced by self-built machine learning-accelerated structural predictions<sup>27,32</sup>. This analysis reveals that La atomic layers are sandwiched between two-dimensional honeycomb planes formed by Cu and Si atoms, with an interlaminar distance of approximately 2.15 Å (Fig. 1e). Prior studies have postulated the presence of anionic electrons nestled within the interstitial spaces between the Cu/Si and La layers, thus lending credence to its nomination as ‘electride’<sup>33</sup>. Further corroborating this, Bader charge analysis of as-constructed IE LaCu<sub>0.67</sub>Si<sub>1.33</sub> model underscores that Cu and Si atoms act as electron acceptors from La atoms, as evidenced by their respective charge states (Fig. 1e, La: 1.14 |e|; Cu: −0.77 |e|; Si: −0.47 |e|). To gain deeper insights, we experimentally delved into the electronic structure of the synthesized IE LaCu<sub>0.67</sub>Si<sub>1.33</sub> material.

The Cu *LMM* spectrum confirms Cu maintains its metallic state in the IE LaCu<sub>0.67</sub>Si<sub>1.33</sub> sample (Supplementary Fig. 4). The high-resolution Cu 2*p* XPS spectra reveal a negative shift in the binding energy of IE LaCu<sub>0.67</sub>Si<sub>1.33</sub> by approximately 0.14 eV compared to pure Cu nanoparticles, suggesting an enhanced electron density in the former (Fig. 1f). This observation is further reinforced by the Cu K-edge spectra of X-ray absorption near-edge structure (XANES) analysis, which displays a lower absorption threshold position and reduced intensity of the white-line peak for IE LaCu<sub>0.67</sub>Si<sub>1.33</sub> material compared to Cu foil (Fig. 1g)<sup>34–36</sup>. The Fourier-transformed *k*<sup>2</sup>-weighted extended X-ray absorption fine-structure (EXAFS) spectrum displayed a weak peak around 2.2 Å (Fig. 1h). Combined with the EXAFS spectrum fitting results, the average Cu–Cu coordination number (CN) in IE LaCu<sub>0.67</sub>Si<sub>1.33</sub> is 1.53, significantly lower than that of Cu foil (Supplementary Fig. 5 and Table S1). Having established the characteristic electride properties of IE LaCu<sub>0.67</sub>Si<sub>1.33</sub>, we move on to explore its behaviors towards WD.

### WD on IE LaCu<sub>0.67</sub>Si<sub>1.33</sub>

First, we used DFT calculations to project energetics of WD on the constructed IE LaCu<sub>0.67</sub>Si<sub>1.33</sub> model (Supplementary Fig. 6). Strikingly, our findings indicate a substantially lower stepwise barrier for the dissociation of \*H<sub>2</sub>O into \*H + \*OH on the (101) surface of IE LaCu<sub>0.67</sub>Si<sub>1.33</sub>, which is the most exposed surface, at 0.33 eV, compared

to the Cu(111) surface, which exhibits a barrier of 1.19 eV. Furthermore, this dissociation pathway was found to be more exergonic on the IE LaCu<sub>0.67</sub>Si<sub>1.33</sub>(101) surface (−1.33 eV), relative to the Cu(111) control (0.29 eV). These theoretical insights, from both thermodynamic and kinetic perspectives, strongly suggest that WD is preferentially facilitated on the surface of IE LaCu<sub>0.67</sub>Si<sub>1.33</sub>, even with the inclusion of solvation energies. (Fig. 2a and Supplementary Fig. 7).

To support the above calculations, H<sub>2</sub>O-temperature-programmed surface reaction (TPSR) tests were further carried out to track WD on various catalysts. Notably, on IE LaCu<sub>0.67</sub>Si<sub>1.33</sub> sample, we first observed a desorption peak at around 84 °C (*m/z* = 18), which can be ascribed to the release of physically adsorbed H<sub>2</sub>O molecules (*m/z* = 18, Fig. 2b). Subsequently, we observed peaks corresponding to the desorption of H<sub>2</sub> (*m/z* = 2) at about 340 and 540 °C. Given that water is the sole source for the adsorbed hydrogen in our test, the above observations indicate that, on the IE LaCu<sub>0.67</sub>Si<sub>1.33</sub> surface, WD occurred below 84 °C at which temperature the molecular H<sub>2</sub>O desorbs from the surface. We also conducted TPSR tests on other control catalysts, including commercial Cu nanoparticles, home-made La<sub>3</sub>Cu<sub>2</sub> and CuSi<sub>2</sub> nanoparticles, and found both have a H<sub>2</sub>O desorption temperature close to 80 °C (Fig. 2b, Supplementary Figs. 8–10). Strikingly, we did not observe any peaks corresponding to H<sub>2</sub> desorption on these materials within the 25–600 °C range tested, aligning with typical TPSR outcomes for conventional Cu-based alloys<sup>37</sup>. In addition, a prominent inelastic scattering background was observed on IE LaCu<sub>0.67</sub>Si<sub>1.33</sub> in the neutron diffraction pattern based on elastic scattering, which is closely related to the presence of hydrogen-containing structure after dehydration treatment (Supplementary. 11). In short, combined results from TPSR tests, neutron diffraction pattern and energetic calculations enable us to conclude an exceptional WD capability of the IE LaCu<sub>0.67</sub>Si<sub>1.33</sub> catalyst, potentially stemming from its distinctive electronic structure inherent to IE materials.

### CO<sub>2</sub>RR performances

The electrolysis of CO<sub>2</sub> on the IE LaCu<sub>0.67</sub>Si<sub>1.33</sub> catalyst was carried out in a flow cell using 1M KOH as the electrolyte. To benchmark the performance, commercial Cu nanoparticles (Supplementary Figs. 12, 13) were adopted, exhibiting comparable electrocatalytic activity and product distribution to previous reports, thereby validating our evaluating system<sup>38</sup>. Notably, the IE LaCu<sub>0.67</sub>Si<sub>1.33</sub> catalyst distinguished itself from the commercial Cu nanoparticles by predominantly producing methane across all investigated current densities, ranging from 100 to 900 mA cm<sup>−2</sup>. Specifically, it reached a peak Faraday efficiency (FE) of 72% at −1.21 V vs. RHE, corresponding to a partial current density (*j*<sub>CH<sub>4</sub></sub>) of 429.7 mA cm<sup>−2</sup> (Fig. 3a). Furthermore, a high *j*<sub>CH<sub>4</sub></sub> of 476.7 mA cm<sup>−2</sup> was achieved at −1.52 V vs. RHE (Fig. 3b), highlighting the exceptional performance of the IE LaCu<sub>0.67</sub>Si<sub>1.33</sub> catalyst. We also noticed the IE

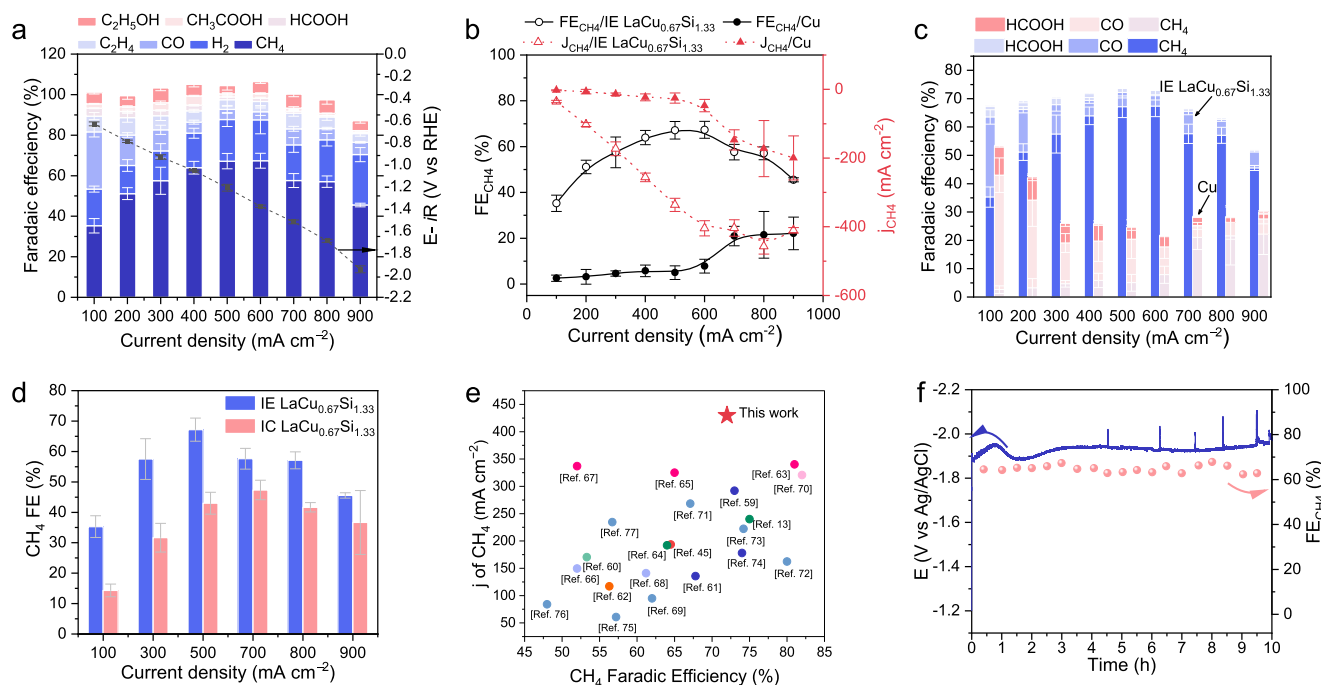


**Fig. 3 | CO<sub>2</sub>RR performance.** **a** The faradaic efficiencies (FE) for various products of IE LaCu<sub>0.67</sub>Si<sub>1.33</sub> and corresponding cathode potentials ( $E - iR$  vs RHE;  $R = 3.49 \pm 0.04$ ) at different applied current densities, the error bars of FEs are calculated based on three independent measurements. **b** FE and partial current densities for CH<sub>4</sub> of IE LaCu<sub>0.67</sub>Si<sub>1.33</sub> and Cu as a function of cathodic currents. The error bars of  $FE_{CH_4}$  and  $j_{CH_4}$  are calculated based on three independent measurements. **c** Comparison of the FE for various C<sub>1</sub> products of IE LaCu<sub>0.67</sub>Si<sub>1.33</sub> and Cu at

different applied current densities. **d** CH<sub>4</sub> FE of IE LaCu<sub>0.67</sub>Si<sub>1.33</sub> and IC LaCu<sub>0.67</sub>Si<sub>1.33</sub> at various current density. **e** Performance comparison regarding selectivity and productivity of CH<sub>4</sub> on the IE LaCu<sub>0.67</sub>Si<sub>1.33</sub> catalyst and prior reports in flow cells. **f** A continuous 10-h CO<sub>2</sub> electrolysis using IE LaCu<sub>0.67</sub>Si<sub>1.33</sub> catalyst under  $-100 \text{ mA cm}^{-2}$ . The CO<sub>2</sub> flow rate was 20 sccm. 1 M KOH was used as the electrolyte. Source data are provided as a Source Data file. <sup>13,45,59–77</sup>

LaCu<sub>0.67</sub>Si<sub>1.33</sub> catalyst efficiently suppressed the generation of other liquid and gaseous products (Supplementary Fig. 14). Within the whole potential region, the total FE of C<sub>1</sub> product on the IE LaCu<sub>0.67</sub>Si<sub>1.33</sub> catalyst is higher than that on commercial Cu nanoparticles, which can be ascribed to a lower paired-Cu-site proportion on the former surface for C–C coupling, as evidenced by the fitting results from XAS analysis (Fig. 3c).

To further inspect the correlation between the IE characteristic and CH<sub>4</sub> selectivity, we crafted a LaCu<sub>0.67</sub>Si<sub>1.33</sub> control sample, which exhibited relatively inferior crystallinity (denoted as IC LaCu<sub>0.67</sub>Si<sub>1.33</sub>) than the IE LaCu<sub>0.67</sub>Si<sub>1.33</sub> sample. This was experimentally achieved by reducing the cycles of electric arc-melting while maintaining the same feeding ratio of La, Cu, and Si elements. In the XRD pattern of IC LaCu<sub>0.67</sub>Si<sub>1.33</sub>, the diffraction peaks observed were consistent with of the main diffraction peaks of IE LaCu<sub>0.67</sub>Si<sub>1.33</sub>, but some stray peaks were also observed (Supplementary Fig. 15). Less obvious lattice fringes, compared to the IE LaCu<sub>0.67</sub>Si<sub>1.33</sub> catalyst, were observed in the TEM selected area of IC LaCu<sub>0.67</sub>Si<sub>1.33</sub>, corroborating the latter's low crystallinity. EDX elemental mappings indicate that La, Cu, and Si are evenly distributed throughout the entire surveyed area (Supplementary Fig. 16). Next, H<sub>2</sub>O-TPSR analysis was performed on the IC LaCu<sub>0.67</sub>Si<sub>1.33</sub> sample to probe its response to WD. The IC LaCu<sub>0.67</sub>Si<sub>1.33</sub> sample exhibited a water desorption peak ( $m/z = 18$ ) at 75 °C and two H<sub>2</sub> desorption peak ( $m/z = 2$ ) at 266 and 384 °C. Comparative integration of the H<sub>2</sub> desorption peaks between the two samples revealed a 1.56-fold increase in peak area for IE LaCu<sub>0.67</sub>Si<sub>1.33</sub>, underscoring the pivotal role of the unique IE feature in enhancing WD on the IE LaCu<sub>0.67</sub>Si<sub>1.33</sub> catalyst (Supplementary Fig. 17). It is worth noting that both the IC LaCu<sub>0.67</sub>Si<sub>1.33</sub> and IE LaCu<sub>0.67</sub>Si<sub>1.33</sub> samples were obtained by ball milling and exhibited comparable specific surface areas, thereby negating the influence of surface area effects (Supplementary Fig. 18 and Table S2). Notably, there are

marked discrepancies in atomic configurations of active sites between IC and IE LaCu<sub>0.67</sub>Si<sub>1.33</sub> surfaces. The disordered atomic arrangement in the IC model likely disrupts the anionic electron characteristics inherent in the crystalline lattice. This structural distortion results in diminished electron transfer capacity to adsorbed \*CO species, as evidenced by the reduced electron transfer (1.23 |e|) compared to the IE surface (1.70 |e|). Consequently, the IC surface exhibits significantly weaker CO adsorption strength, with an adsorption energy of  $-1.49 \text{ eV}$  versus  $-2.27 \text{ eV}$  for the IE surface, highlighting the critical relationship between the IE characteristics and catalytic performance (Supplementary Fig. 19). Applying the IC LaCu<sub>0.67</sub>Si<sub>1.33</sub> catalyst for CO<sub>2</sub> electrolysis, we found a lower FE of methane than IE LaCu<sub>0.67</sub>Si<sub>1.33</sub> across the whole investigated current densities (Fig. 3d and Supplementary Fig. 20). Consequently, the above structural and electrochemical results strongly suggest a correlation between the IE features, facilitated WD and enhanced CH<sub>4</sub> selectivity on the IE LaCu<sub>0.67</sub>Si<sub>1.33</sub> catalyst.

By comparing with prior representative methanization catalysts and home-made La<sub>3</sub>Cu<sub>2</sub> and CuSi<sub>2</sub> nanoparticles in flow cell setups under alkaline electrolyte, our IE LaCu<sub>0.67</sub>Si<sub>1.33</sub> catalyst demonstrated significant advancements in both selectivity and partial current density (Fig. 3e, Supplementary Fig. 21–23). We also conducted an initial evaluation of structural stability of this new material as methanization electrocatalyst by operating the IE LaCu<sub>0.67</sub>Si<sub>1.33</sub> catalyst in a flow cell for a continuous 10-h electrolysis at  $-100 \text{ mA cm}^{-2}$ . Throughout this duration, both the applied potential and the selectivity of CH<sub>4</sub> remained stable, with minimal fluctuations observed (Fig. 3f). From the respective STEM images and XRD patterns of IE LaCu<sub>0.67</sub>Si<sub>1.33</sub> catalyst before and after CO<sub>2</sub> electrolysis, we observed negligible variations in either morphology or crystallinity, indicative of its structural integrity throughout the electrolysis process (Supplementary Fig. 24).



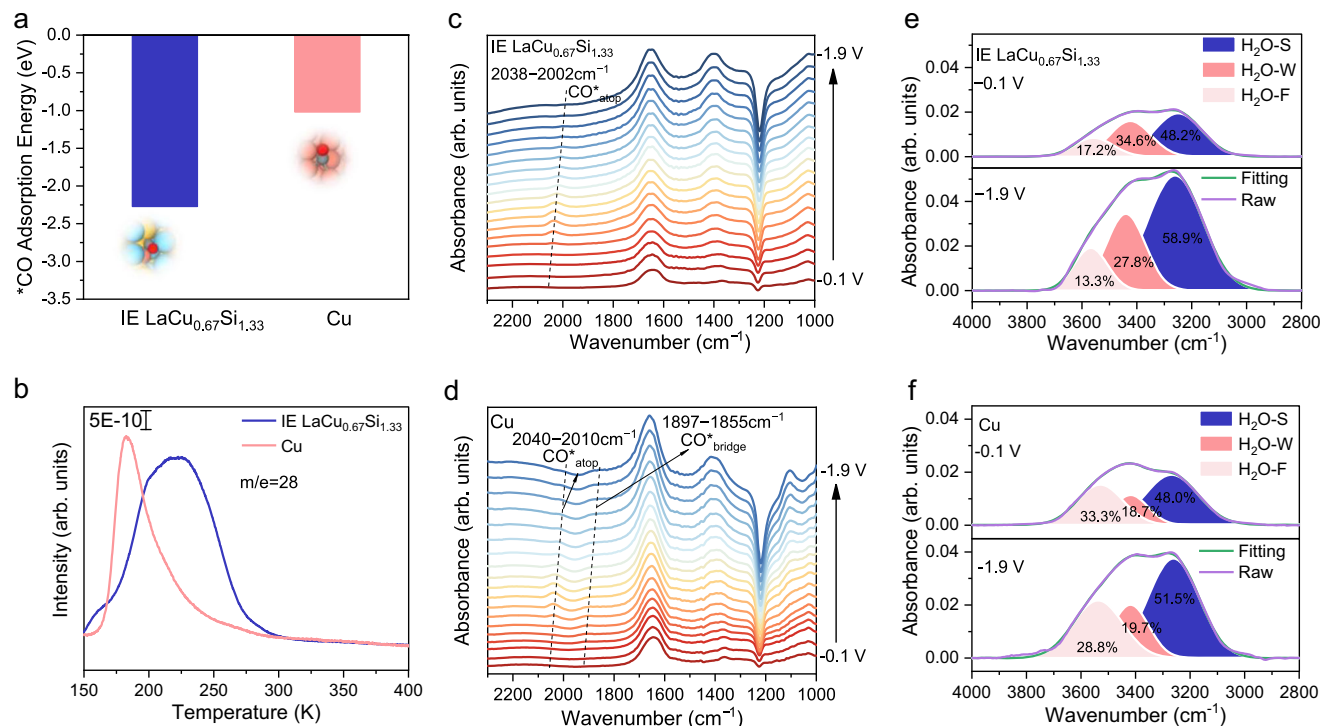


**Fig. 4 | Analysis of intermediate adsorptions.** **a** Calculated adsorption energies of  $^*CO$  on IE LaCu<sub>0.67</sub>Si<sub>1.33</sub>(101) and Cu(111) surfaces. **b** Low temperature CO-temperature program desorption curves over the IE LaCu<sub>0.67</sub>Si<sub>1.33</sub> and Cu catalysts. Single of  $m/e = 28$  is CO. **c, d** In situ ATR-SEIRAS spectra of IE LaCu<sub>0.67</sub>Si<sub>1.33</sub> and Cu in

CO<sub>2</sub>-saturated 0.5 M KHCO<sub>3</sub> electrolyte at the applied potential of -0.1 to -1.9 V. **e, f** Deconvolution of the experimental O-H stretching vibration peak at -0.1 V and -1.9 V in IE LaCu<sub>0.67</sub>Si<sub>1.33</sub> and Cu samples. Source data are provided as a Source Data file.

## Mechanistic studies

In literature, the energetics of  $^*CO$  has been widely used to project the electrocatalytic outcomes of CO<sub>2</sub> into various mono-carbon or multi-carbon products<sup>39</sup>. Specifically, for the methanation of CO<sub>2</sub>,  $^*CO$  undergoes an additional six hydrogenation steps, necessitating a robust methanization catalyst with substantial CO binding energy to hinder its undesirable desorption as a byproduct. Therefore, we initiated our mechanistic investigations by comparing the adsorption energies of  $^*CO$  on the IE LaCu<sub>0.67</sub>Si<sub>1.33</sub> and Cu surfaces using DFT calculations. CO has a significantly more negative adsorption energy on IE LaCu<sub>0.67</sub>Si<sub>1.33</sub>(101) than on Cu(111) (-2.27 vs. -1.02 eV), indicative of a more stable adsorption of  $^*CO$  on the former (Fig. 4a). To validate these theoretical predictions, we employed low temperature CO-TPD experiments, which corroborated our DFT results by demonstrating that the IE LaCu<sub>0.67</sub>Si<sub>1.33</sub> catalyst exhibits a higher CO desorption temperature than Cu nanoparticles (220 vs. 180 K). Moreover, the larger CO desorption peak area on the IE LaCu<sub>0.67</sub>Si<sub>1.33</sub> surface, which is 2.6 times that of Cu nanoparticles, underscores the higher coverage of  $^*CO$  on the former (Fig. 4b and Supplementary Fig. 25).

We further performed in situ attenuated total reflectance surface-enhanced infrared absorption spectroscopy (ATR-SEIRAS) to probe the adsorption characteristics of CO during the reaction. On the IE LaCu<sub>0.67</sub>Si<sub>1.33</sub>, we observed a distinct signal in the range of 2038–2002 cm<sup>-1</sup>, attributed to linearly atop-adsorbed CO ( $^*CO_{atop}$ ). However, on the control Cu nanoparticles, in situ ATR-SEIRAS shows two prominent peaks for  $^*CO_{atop}$  at 2040–2010 cm<sup>-1</sup> and bridge-adsorbed CO ( $^*CO_{bridge}$ ) at 1897–1855 cm<sup>-1</sup>, respectively<sup>40</sup> (Fig. 4c, d). Notably, the peak associated with the  $^*CO_{atop}$  on Cu nanoparticles displays a blue-shift compared with that on the IE LaCu<sub>0.67</sub>Si<sub>1.33</sub>. This shift can be explained by the back-donation of electrons from the metal Cu atoms on the IE LaCu<sub>0.67</sub>Si<sub>1.33</sub> surface, which enhances the filling of the 2π orbital of the CO molecule with electrons. This observation suggests the increased electronegativity of Cu atoms on the IE LaCu<sub>0.67</sub>Si<sub>1.33</sub>

surface, aligning with our calculations. The IE LaCu<sub>0.67</sub>Si<sub>1.33</sub> exhibits a significantly higher  $^*CO_{atop}$  peak intensity compared to pure Cu across the entire potential window studied that can be attributed to the substantial difference in CO consumption between C<sub>2</sub> and C<sub>1</sub> product formation pathways where C<sub>2</sub> production requires approximately twice the amount of CO compared to C<sub>1</sub> products. Additionally, the presence of a second set of peaks on pure Cu nanoparticles at 1897–1855 cm<sup>-1</sup> corresponds to  $^*CO_{bridge}$  on adjacent Cu sites which related to the coupling behavior of  $^*CO$ . The absence of such  $^*CO_{bridge}$  on the IE LaCu<sub>0.67</sub>Si<sub>1.33</sub> aligns with its tendency to favor C<sub>1</sub> products and reinforces our EXAFS findings that this catalyst exhibits significantly lower Cu-Cu coordination numbers compared to pure Cu nanoparticles.

Recent evidence verified the pivotal role of interfacial water in the electrocatalysis of HER and CO<sub>2</sub>RR<sup>41</sup>, which prompts us to investigate the interfacial water structures close to the IE LaCu<sub>0.67</sub>Si<sub>1.33</sub> and Cu nanoparticles using ATR-SEIRAS. Our spectroscopic results revealed a broad vibrational band corresponding to V(O-H) stretching, spanning 3700 to 3000 cm<sup>-1</sup> on both catalysts. This band is typically ascribed to diverse O-H stretching modes of water, encompassing signals from free water (H<sub>2</sub>O-F), strongly hydrogen-bonded water (H<sub>2</sub>O-S), and weakly hydrogen-bonded water (H<sub>2</sub>O-W), as corroborated by previous literature (Supplementary Fig. 26)<sup>42–44</sup>. Notably, as the potential increased, the proportions of H<sub>2</sub>O-F and H<sub>2</sub>O-W peaks on both IE LaCu<sub>0.67</sub>Si<sub>1.33</sub> and Cu decreased, concurrent with the Stark effect. In principle, H<sub>2</sub>O-F and H<sub>2</sub>O-W are energetically easier to be dissociated for hydrogenation compared to H<sub>2</sub>O-S. It is therefore reasonable to deduce that a catalyst with strong water-dissociation capabilities should manifest a lower ratio of H<sub>2</sub>O-F and H<sub>2</sub>O-W peaks, as these species are expected to be consumed rapidly. Consistent with this rationale, the IE LaCu<sub>0.67</sub>Si<sub>1.33</sub> catalyst exhibited a notably lower ratio of H<sub>2</sub>O-F and H<sub>2</sub>O-W peak areas compared to the control Cu nanoparticles, highlighting the superior water-dissociation

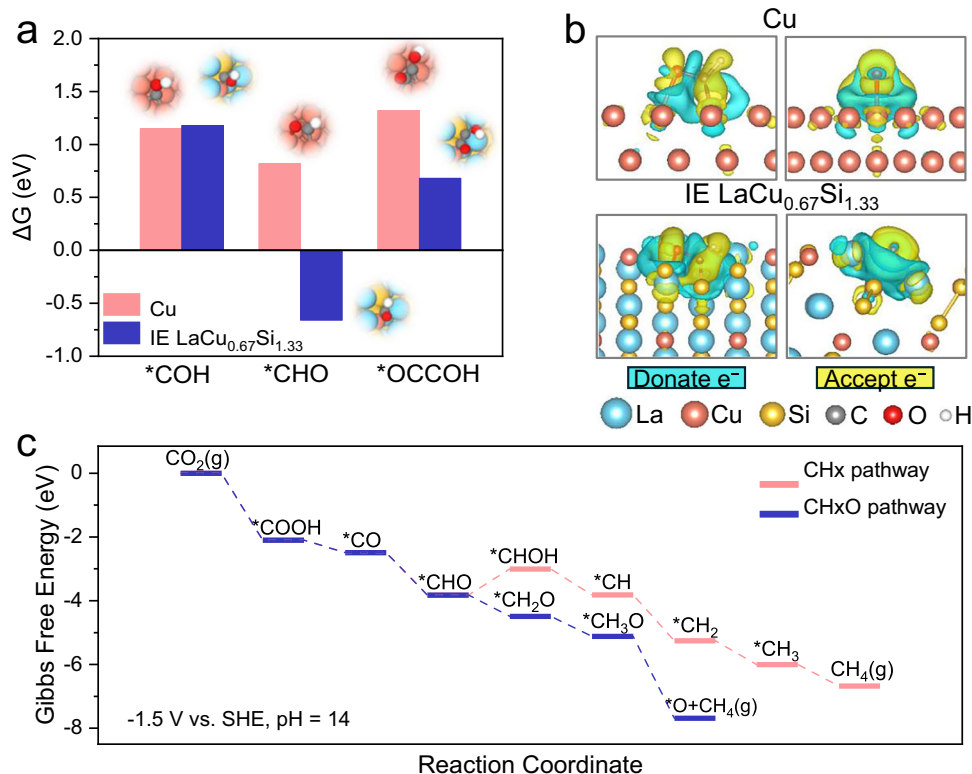


**Fig. 5 | DFT calculations.** **a** Hydrogenation and C–C coupling energies of  $\text{*CO}$  intermediate on IE  $\text{LaCu}_{0.67}\text{Si}_{1.33}$ (101) and Cu(111) surfaces. **b** Side view of charge-density differences of  $\text{*CHO}$  intermediate on IE  $\text{LaCu}_{0.67}\text{Si}_{1.33}$ (101) and Cu(111)

surfaces. **c** Gibbs free energy diagram of two  $\text{CO}_2$ -to- $\text{CH}_4$  pathways on the IE  $\text{LaCu}_{0.67}\text{Si}_{1.33}$ (101) surface. Source data are provided as a Source Data file.

properties of the former (Figure e, f and Supplementary Fig. 27). To quantify this difference, we compared the integration of the adsorption peaks at  $-0.1$  V and  $-1.9$  V, and found that the consumption of  $\text{H}_2\text{O}$ –F and  $\text{H}_2\text{O}$ –W peaks on IE  $\text{LaCu}_{0.67}\text{Si}_{1.33}$  was approximately three times that on Cu nanoparticles, further confirming the exceptional WD capability of the IE  $\text{LaCu}_{0.67}\text{Si}_{1.33}$  catalyst (Supplementary Fig. 28).

To theoretically rationalize the high  $\text{CH}_4$  selectivity of IE  $\text{LaCu}_{0.67}\text{Si}_{1.33}$  catalyst, we carried out DFT calculations to investigate the methanogenesis pathways. After the adsorption of  $\text{CO}$ , the energy levels of  $\text{CO}$  protonation and C–C coupling determine the branching of  $\text{C}_1$  (e.g.,  $\text{CH}_4$ ,  $\text{CH}_3\text{OH}$ ) vs.  $\text{C}_2$  (e.g.,  $\text{C}_2\text{H}_4$ ,  $\text{C}_2\text{H}_5\text{OH}$ ) products. Therefore, we first compared the changes of Gibbs free energy for  $\text{CO}$  protonation and C–C coupling pathways (Fig. 5a). We found that the C–C coupling on the IE  $\text{LaCu}_{0.67}\text{Si}_{1.33}$ (101) surface is significantly energetically unfavorable compared to its protonation ( $0.68$  vs.  $-0.66$  eV), and  $\text{*CO}$  undergoes hydrogenation with a preference to form  $\text{*CHO}$  rather than  $\text{*COH}$  ( $-0.66$  vs.  $1.18$  eV), even with a contribution of solvation (Supplementary Fig. 29). In contrast, although the protonation of  $\text{*CO}$  to  $\text{*CHO}$  is also energetically preferred on the Cu(111) surface, there is a small difference in energy between  $\text{CO}$  protonation and C–C coupling ( $0.82$  vs.  $1.32$  eV). These calculated results are consistent with our ATR-SEIRAS observations. The charge density distributions were analyzed for both IE  $\text{LaCu}_{0.67}\text{Si}_{1.33}$  and Cu surfaces with adsorbed  $\text{*CHO}$  by comparing the electron charge donation/acceptance status (Fig. 5b). After the adsorption of  $\text{*CHO}$ , the donation of electron charge can be observed on both IE  $\text{LaCu}_{0.67}\text{Si}_{1.33}$ (101) and Cu(111) surfaces, and the electron charge is accumulated between  $\text{*CHO}$  and surfaces. However, the electron density of the IE  $\text{LaCu}_{0.67}\text{Si}_{1.33}$ (101) surface, which is composed of transition metals with strongly changed charge states and anionic electrons, is stronger than that of Cu(111). Specifically, the IE  $\text{LaCu}_{0.67}\text{Si}_{1.33}$  surface has more electrons that can be transferred to

$\text{*CHO}$  than the Cu surface ( $1.74$  vs.  $0.39$  | $e^-$ |), which explains why the IE  $\text{LaCu}_{0.67}\text{Si}_{1.33}$  surface can adsorb the key intermediate  $\text{*CHO}$  more stable than the Cu surface ( $-4.25$  vs.  $-1.51$  eV) to efficiently promote the  $\text{CH}_4$  selectivity.

Figure 5c further provides the Gibbs free energy diagram for converting  $\text{CO}_2$  to  $\text{CH}_4$  on the IE  $\text{LaCu}_{0.67}\text{Si}_{1.33}$  surface through the  $\text{*CHO}$  intermediate and possible hydrogenation routes according to previous literature<sup>45</sup>. The adsorption configurations of the related intermediates are given in Supplementary Fig. 30. The formation of  $\text{*COOH}$  and  $\text{*CHO}$  are exergonic on the IE  $\text{LaCu}_{0.67}\text{Si}_{1.33}$  surface ( $-2.1$  and  $-1.33$  eV) but endergonic on the Cu surface ( $0.15$  and  $0.15$  eV), which contributes to the higher  $\text{CH}_4$  selectivity of IE  $\text{LaCu}_{0.67}\text{Si}_{1.33}$ . The further hydrogenation products of  $\text{*CHO}$  can be  $\text{*CH}_2\text{O}$  or  $\text{*CHOH}$ . By comparing the Gibbs free energies of these two pathways, we found that the hydrogenation of  $\text{*CHO}$  to  $\text{*CH}_2\text{O}$  is more favored. The consecutive hydrogenation of the C end of  $\text{*CH}_2\text{O}$  is strong exergonic, forming  $\text{CH}_4$ . The effect of solvation energies on reaction free energies was benchmarked, proving that calculated results capture the correct trends (Supplementary Figs. 31, 32). We proposed that the  $\text{CO}_2$ -to- $\text{CH}_4$  conversion on the IE  $\text{LaCu}_{0.67}\text{Si}_{1.33}$  surface follows:  $\text{CO}_2 \rightarrow \text{*COOH} \rightarrow \text{*CO} \rightarrow \text{*CHO} \rightarrow \text{*CH}_2\text{O} \rightarrow \text{*CH}_3\text{O} \rightarrow \text{CH}_4$  (Supplementary Figs. 33, 34).

## Discussion

In summary, we have reported a class of IE  $\text{LaCu}_{0.67}\text{Si}_{1.33}$  catalyst with spontaneous WD for enhanced electrosynthesis of methane from  $\text{CO}_2$  reduction. Based on a series of physical characterizations and theoretical projections, we have unveiled the distinct electronic structures of IE  $\text{LaCu}_{0.67}\text{Si}_{1.33}$  catalyst. The behaviors of WD on various catalysts were systematically investigated employing both experimental and calculational means, the results of which underscore a significantly enhanced WD on IE  $\text{LaCu}_{0.67}\text{Si}_{1.33}$  over other control catalysts, including pure Cu and typical solid-solution alloys. We have evaluated

this IE LaCu<sub>0.67</sub>Si<sub>1.33</sub> catalyst for CO<sub>2</sub> reduction in an alkaline flow cell, and achieved a remarkable methane Faraday efficiency of 72% at −1.21 V vs. RHE and the highest partial current density of 476.7 mA cm<sup>−2</sup>, along with an initial durability for 10 h. The coupling of in situ spectroscopies and DFT calculations pained an energetically favorable reaction pathway for the CO<sub>2</sub>-to-CH<sub>4</sub> conversion on the IE LaCu<sub>0.67</sub>Si<sub>1.33</sub> surface. This work demonstrates the spontaneous WD capability of IE materials as a promising catalyst platform for the electrochemical methanization of CO<sub>2</sub> and potentially other H<sub>2</sub>O-involved renewable conversions.

## Methods

### Chemicals and materials

La, Cu and Si ingots (with a purity of 99.9%) were purchased from Cuibolin Instruments Ltd., Beijing. Commercial Cu nanoparticles (25 nm) were purchased from Sigma Aldrich. Gold chloride trihydrate (HAuCl<sub>4</sub>·3H<sub>2</sub>O, 99%), sodium hydroxide (NaOH, AR), potassium hydroxide (KOH, 85%), hydrofluoric acid (HF, 2%), ammonium fluoride (NH<sub>4</sub>F, AR), sodium thiosulfate (Na<sub>2</sub>S<sub>2</sub>O<sub>3</sub>, AR), sodium sulfite (Na<sub>2</sub>SO<sub>3</sub>, AR), sulfuric acid (H<sub>2</sub>SO<sub>4</sub>, 98%), ammonium chloride (NH<sub>4</sub>Cl, AR) and Acetone was purchased from Sinopharm group reagent Co. Ltd. The carbon paper-based gas diffusion layers (GDLs, Sigracet 28BC), anion-exchange membrane (AEM, Fumasep FAA-3-PK-130) and D520 Nafion™ dispersion (5 wt%) were purchased from fuel cell store. Ultrapure Millipore water (resistivity 18.2 MΩcm) was used for all experiments. High purity CO<sub>2</sub> gas (99.99%) was purchased from Tianjin liquefied gas Co. Ltd. All chemicals were purchased from commercial suppliers and used without further purification.

### Synthesis of IE LaCu<sub>0.67</sub>Si<sub>1.33</sub> catalyst

The IE LaCu<sub>0.67</sub>Si<sub>1.33</sub> sample was synthesized through arc-melting stoichiometric ratios of La, Cu, and Si ingots in a water-cooled copper furnace under purified argon atmosphere (about −5 bar). To ensure phase purity, the arc-melting process was repeated eight times with intermediate flipping of the ingot. The resulting bulk material was manually ground into coarse powder using an agate mortar, followed by high-energy ball milling at 200 rpm for 20 h employing a ball-to-powder mass ratio of 20: 1 to achieve nanoparticle refinement. Wet milling with water was utilized during this size reduction process.

### Synthesis of IC LaCu<sub>0.67</sub>Si<sub>1.33</sub>, La<sub>3</sub>Cu<sub>2</sub> and CuSi<sub>2</sub> catalysts

The IC LaCu<sub>0.67</sub>Si<sub>1.33</sub> was prepared following identical procedures but with a single arc-melting cycle. Similarly, La<sub>3</sub>Cu<sub>2</sub> and CuSi<sub>2</sub> were synthesized using equivalent methodology, where respective elemental combinations (La + Cu or Cu + Si) were arc-melted in stoichiometric proportions under identical reactor conditions.

### Characterizations

X-ray diffraction (XRD) patterns were obtained on a Bruker D2 Advance powder diffractometer with Cu-Kα radiation ( $\lambda = 1.54178 \text{ \AA}$ ) at 30 kV and 10 mA. Imaging and elemental mapping were recorded on a field emission transmission electron microscope (TEM, JEOL ARM-200 F) equipped with a cold field emission gun and dual energy-dispersive X-ray detectors, operating at 200 kV accelerating voltage. The JEOL ARM200F microscope, equipped with an aberration corrector and dual energy-dispersive X-ray detectors, was used for high-resolution high-angle annular dark-field scanning transmission electron microscopy (HAADF-STEM) imaging and corresponding elemental mapping. X-ray photoelectron spectroscopy (XPS) measurements were performed on a Thermo Scientific K-alpha system with an exciting source of Al Kα. The binding energy was calibrated using the extrinsic carbon C 1s peak (284.6 eV). The textural properties of the samples were determined from N<sub>2</sub>-sorption isotherms recorded on a Micromeritics ASAP 2460 instrument at 77 K. The H<sub>2</sub>O-temperature-programmed surface reaction (TPSR) curves

were recorded using a Micromeritics ChemiSorb 2920 instrument equipped with an online mass spectrometer. 300 mg of the sample was loaded into a U-tube, with He as the carrier gas (50 mL min<sup>−1</sup>), and heated to 600 °C for 2 h to remove surface residues. After cooling the sample to room temperature, water vapor was introduced over the catalyst surface via the He flow. The He flow was maintained at room temperature for 30 min to eliminate any excess H<sub>2</sub>O. Finally, TPSR measurements were conducted from 30 °C to 600 °C under helium at a heating rate of 10 °C min<sup>−1</sup>. For low-temperature CO-TPD, the sample was heated to 600 °C and held for 2 h in Ar atmosphere, followed by a switch to He gas at the same temperature for additional 30 min. After cooling to room temperature, the sample was further reduced to 150 K using liquid nitrogen circulation, and the carrier gas was switched back to the 5% CO-He mixture. Once the baseline stabilized, the data curve was recorded during heating from 150 K to 400 K at a rate of 20 K min<sup>−1</sup>. Powder neutron data were collected on the Multi-physics instrument at China Spallation Neutron Source (CSNS), Dongguan, China. Before testing, the sample IE LaCu<sub>0.67</sub>Si<sub>1.33</sub> underwent a three-stage treatment process: First, it was thermally annealed at 600 °C for 2 h under continuous argon flow. Following cooling to ambient temperature, the atmosphere was switched to a water vapor-saturated argon flow (maintained for 1 h). Finally, the system was purged with pure argon and subjected to a secondary thermal treatment at 300 °C for 2 h to complete the processing. The sample (ca. 2 g) was loaded in vanadium alloy cans in the glove box. Then the powder neutron data were conducted by multiple bank detectors at room temperature.

### Preparation of gas diffusion electrodes

A catalyst ink was prepared by ultrasonically 8 mg of catalyst powder with 20 μL of Nafion solution (≈5 wt.%) in 1 mL ethanol for 1 h to achieve homogeneous dispersion. This ink was then uniformly spray-coated onto the microporous carbon layer of a 4 × 4 cm<sup>2</sup> carbon paper substrate (Sigracet 28BC) using an airbrush system. The catalyst loading was controlled at approximately 0.35 mg cm<sup>2</sup>, as determined by gravimetric analysis of the substrate before and after coating. The coated electrode was trimmed to expose a 1 × 1 cm<sup>2</sup> active area of catalytic layer. Finally, the prepared GDE was air-dried under ambient conditions for 12 h prior to electrochemical testing.

### Electrochemical measurements

The CO<sub>2</sub>RR performance was evaluated at room temperature (25 ± 2 °C) and pressure (1.01 × 10<sup>5</sup> Pa) using a flow cell system, in which the anode and cathode chambers were separated by an ion-conducting anion exchange membrane (Fumasep FAA-3-PK-130). An electrochemical workstation (Autolab PGSTAT204) was configured as a three-electrode system with a constant current source. Anion exchange membrane (2.5 × 2.5 cm<sup>2</sup>) was soaked in 1 M KOH for 48 h and rinsed with deionized water before use. The catalyst loaded GDE served as the working electrode, while an Ag/AgCl electrode (with saturated KCl as the filling solution) and nickel foam were used as the reference and counter electrodes, respectively. All potentials in this experiment were calibrated to the potential relative to the reversible hydrogen electrode (RHE) based on the following equation after IR compensation:

$$E(\text{vs. RHE}) = E(\text{vs. Ag/AgCl}) + 0.197 + 0.059 \times \text{pH} + 0.8 \times iR$$

The 80% *iR* compensation was performed for the electrolysis experiment at each potential, with the ohmic resistance determined through extrapolation of the high-frequency intercept in electrochemical impedance spectra. The Ag/AgCl reference electrode potential was calibrated against the reversible hydrogen electrode (RHE, Phychemi Co., Ltd.) in 1 M KOH electrolyte, yielding a stable value of 1.00 ± 0.01 V vs. RHE. The electrochemical measurements employed a freshly prepared 1 M KOH electrolyte (pH = 13.7 ± 0.2) that



was utilized within 72 h of preparation. The electrolyte was stored in PTFE containers under ambient temperature conditions ( $25 \pm 2^\circ\text{C}$ ) between experimental sessions. For each electrolysis experiment, 10 mL electrolyte were dispensed into both the cathodic and anodic chambers of the flow cell system, each featuring a  $1\text{ cm}^3$  working volume. Continuous electrolyte circulation was maintained through both electrode compartments using a peristaltic pump operating at a constant flow rate of  $10\text{ mL min}^{-1}$ . The high-purity  $\text{CO}_2$  (99.99%) gas supply flow rate was regulated by a mass flow meter and passed through the gas chamber of the flow cell at a flow rate of 20 sccm. Use a stopwatch to time the volume flow rate of the outlet gas through the soap film. The outlet gas was collected in a gas sampling bag (100 mL) and quantitatively analyzed by gas chromatograph (Agilent 7890B).  $\text{CH}_4$  and  $\text{C}_2\text{H}_4$  were detected by flame ionization detector (FID), and  $\text{H}_2$  and CO were detected by thermal conductivity detector (TCD). After the electrolysis, the cathode liquid phase product was analyzed by high performance liquid chromatography (HPLC). The gas and liquid phase products were calibrated by external standard method.

The Faradaic efficiencies (FE) of gas products can be calculated as below:

$$FE_x = \frac{F \times n_x \times V_{\text{gas}} \times c_x}{i \times V_m}$$

Among them,  $F$  denotes the Faraday constant ( $96,485\text{ C mol}^{-1}$ ),  $n_x$  denotes the number of electrons transferred for producing 1 mole of product  $x$ ,  $V_{\text{gas}}$  is the gas flow rate at the flow cell outlet (sccm),  $c_x$  represents the volume concentration of product  $x$  measured by gas chromatography,  $i$  is the total current, and  $V_m$  is the molar volume ( $24.5\text{ L mol}^{-1}$ ;  $298.15\text{ K}$ ).

The FE of liquid products can be calculated as below:

$$FE_x = \frac{F \times n_x \times m_x}{i \times t}$$

Where  $m_x$  represents the amount of liquid products in moles, and  $t$  denotes the electrolysis time (s).

The partial current density for a given product was calculated as:

$$j_x = \frac{i \times FE_x}{\text{electrode area}}$$

## XAFS analysis

XAFS spectroscopic measurements of K-edges for Cu of IE  $\text{LaCu}_{0.67}\text{Si}_{1.33}$  samples were conducted at the BL17B1 and BL20U beamlines in Shanghai Synchrotron Radiation Facility (SSRF). Spectra were collected in transmission mode using a Pilatus detector. For Cu K-edge measurements, Cu foil reference was scanned simultaneously with the sample for energy calibration. The acquired EXAFS data were processed according to the standard procedures using the Athena and Artemis software, parts of the Demeter package. Preprocessing of data included alignment, edge calibration, deglitching, normalization, background subtraction, and conversion of data into a chi file for data fitting; all this was done with Athena; EXAFS of the Cu was fitted to obtain the amplitude reduction factor  $S_0^2$ .

## Theoretical calculations

All calculations were performed using density functional theory (DFT) with the projector augmented wave (PAW)<sup>46,47</sup> method and the Perdew-Burke-Ernzerhof generalized gradient approximation (GGA-PBE)<sup>48</sup>, as implemented in the Vienna Ab Initio Simulation Package (VASP)<sup>49,50</sup>. The cutoff energy was set to 400 eV after a series of tests. The Methfessel-Paxton<sup>51</sup> method with  $\sigma = 0.2\text{ eV}$  was chosen as the smearing algorithm. The electronic self-consistent iteration and atomic forces were converged to within  $10^{-5}\text{ eV}$  and  $0.03\text{ eV \AA}^{-1}$ , respectively. Grimme's DFT-D3<sup>52</sup> approach was adopted to account for dispersion interactions. The optimized bulk lattice constants of IE  $\text{LaCu}_{0.67}\text{Si}_{1.33}$  with  $(5 \times 5 \times 4)$  Monkhorst-Pack  $k$ -point grids<sup>53</sup> are  $a = b = 8.20\text{ \AA}$  and  $c = 12.87\text{ \AA}$ . Convergence tests were performed with respect to the layer thickness and size of constrained layers according to the adsorption energy of  $^*\text{CO}$ . Thus, the adsorption calculations on the IE  $\text{LaCu}_{0.67}\text{Si}_{1.33}$ (101) were performed using a ten-layer  $p(2 \times 1)$  supercell (bottom five layers constrained) containing a vacuum region of  $20\text{ \AA}$

with  $(2 \times 2 \times 1)$  Monkhorst-Pack  $k$ -point grids. The adsorption calculations on the Cu(111) were performed using a six-layer  $p(4 \times 4)$  supercell (bottom three layers constrained) containing a vacuum region of  $20\text{ \AA}$  with  $(3 \times 3 \times 1)$  Monkhorst-Pack  $k$ -point grids. The adsorption energy ( $E_{\text{ads}}$ ) of species  $X$  was calculated by  $E_{\text{ads}} = E_{X/\text{slab}} - E_{\text{slab}} - E_X$ , where  $E_X$ ,  $E_{\text{slab}}$ , and  $E_{X/\text{slab}}$  are the total energy of the free adsorbate in gas phase, clean slab, and slab with the adsorbate, respectively. For reaction steps involving  $\text{H}^+$  and  $\text{e}^-$ , the computational hydrogen electrode (CHE)<sup>54,55</sup> model was used to calculate the Gibbs free energies changes. The thermal corrections to the Gibbs free energies were obtained using VASPKIT tool<sup>56</sup>. The transition state of a chemical reaction was located using the climbing image nudged elastic band method<sup>57</sup>. The electrochemical barriers were evaluated through the scheme developed by Akhade et al.<sup>58</sup>. For all calculations, the optimized structures are provided in Supplementary Data 1.

## In situ IR measurements

In situ IR spectra were collected using a custom three-electrode H electrolytic cell on a Vertex70 (Bruker) spectrophotometer in an internal reflection configuration (Supplementary Fig. 35). Prior to testing, a polished silicon prism substrate was functionalized with a chemically deposited uniform gold film serving as the reflective working electrode. A catalyst ink was prepared by ultrasonically homogenizing 2 mg of catalyst powder with 500  $\mu\text{L}$  ethanol and 10  $\mu\text{L}$  Nafion solution (5 wt%), which was subsequently spray-coated onto the gold film to create a uniform catalytic layer. All electrochemical measurements were performed in  $\text{CO}_2$ -saturated  $0.5\text{ M KHCO}_3$  ( $\text{pH} = 7.4 \pm 0.3$ ) electrolyte, and  $\text{CO}_2$  was continuously bubbled onto the catalyst surface at a flow rate of 10 sccm. All spectra were absorption spectra collected at a resolution of  $4\text{ cm}^{-1}$ , and data were collected at different voltages.

## Data availability

All data generated in this study are provided in the Supplementary Information/Source data file. Source data are provided in this paper. Source data are provided with this paper.

## References

- Gao, D. et al. Rational catalyst and electrolyte design for  $\text{CO}_2$  electroreduction towards multicarbon products. *Nat. Catal.* **2**, 198 (2019).
- Lees, E. W. et al. Gas diffusion electrodes and membranes for  $\text{CO}_2$  reduction electrolyzers. *Nat. Rev. Mater.* **7**, 55 (2022).
- Zhu, H. J. et al. Oxygen-tolerant  $\text{CO}_2$  electroreduction over covalent organic frameworks via photoswitching control oxygen passivation strategy. *Nat. Commun.* **15**, 1479 (2024).
- Fang, W. et al. Durable  $\text{CO}_2$  conversion in the proton-exchange membrane system. *Nature* **626**, 86 (2024).
- Jiang, M. et al. Review on strategies for improving the added value and expanding the scope of  $\text{CO}_2$  electroreduction products. *Chem. Soc. Rev.* **53**, 5149 (2024).
- Ross, M. B. et al. Designing materials for electrochemical carbon dioxide recycling. *Nat. Catal.* **2**, 648 (2019).
- Nitopi, S. et al. Progress and perspectives of electrochemical  $\text{CO}_2$  reduction on copper in aqueous electrolyte. *Chem. Rev.* **119**, 7610 (2019).
- Sun, X. et al. Advancing electrocatalytic reactions through mapping key intermediates to active sites via descriptors. *Chem. Soc. Rev.* **53**, 7392 (2024).
- Seh, Z. et al. Combining theory and experiment in electrocatalysis: Insights into materials design. *Science* **355**, eaad4998 (2017).
- Jiao, J. et al. Constructing asymmetric double-atomic sites for synergistic catalysis of electrochemical  $\text{CO}_2$  reduction. *Nat. Commun.* **14**, 6164 (2023).



11. Chen, J. et al. Promoting CO<sub>2</sub> electroreduction kinetics on atomically dispersed monovalent Zn<sup>I</sup> sites by rationally engineering proton-feeding centers. *Angew. Chem. Int. Ed.* **61**, e202111683 (2022).
12. Jiao, J. et al. Copper atom-pair catalyst anchored on alloy nanowires for selective and efficient electrochemical reduction of CO<sub>2</sub>. *Nat. Chem.* **11**, 222 (2019).
13. Chen, S. et al. Engineering water molecules activation center on multisite electrocatalysts for enhanced CO<sub>2</sub> methanation. *J. Am. Chem. Soc.* **144**, 12807 (2022).
14. Li, Y. et al. Promoting CO<sub>2</sub> methanation via ligand-stabilized metal oxide clusters as hydrogen-donating motifs. *Nat. Commun.* **11**, 6190 (2020).
15. Ma, M. et al. Local reaction environment for selective electroreduction of carbon monoxide. *Energy Environ. Sci.* **15**, 2470 (2022).
16. Sa, Y. et al. Catalyst–electrolyte interface chemistry for electrochemical CO<sub>2</sub> reduction. *Chem. Soc. Rev.* **49**, 6632 (2020).
17. Liu, X. et al. Understanding trends in electrochemical carbon dioxide reduction rates. *Nat. Commun.* **8**, 15438 (2017).
18. Zhi, X., Vasileff, A., Zheng, Y., Jiao, Y. & Qiao, S. Role of oxygen-bound reaction intermediates in selective electrochemical CO<sub>2</sub> reduction. *Energy Environ. Sci.* **14**, 3912 (2021).
19. Dinh, C. T. et al. Multi-site electrocatalysts for hydrogen evolution in neutral media by destabilization of water molecules. *Nat. Energy* **4**, 107 (2019).
20. Subbaraman, R. et al. Trends in activity for the water electrolyser reactions on 3d M(Ni,Co,Fe,Mn) hydr(oxy)oxide catalysts. *Nat. Mater.* **11**, 550 (2012).
21. Luo, M. et al. Hydroxide promotes carbon dioxide electroreduction to ethanol on copper via tuning of adsorbed hydrogen. *Nat. Commun.* **10**, 5814 (2019).
22. Zhang, Q. et al. Atomic dynamics of electrified solid–liquid interfaces in liquid-cell TEM. *Nature* **630**, 643 (2024).
23. Yang, Y. et al. Operando studies reveal active Cu nanograins for CO<sub>2</sub> electroreduction. *Nature* **614**, 262 (2023).
24. Amirbeigiab, R. et al. Atomic-scale surface restructuring of copper electrodes under CO<sub>2</sub> electroreduction conditions. *Nat. Catal.* **6**, 837 (2023).
25. Vavra, J. et al. Solution-based Cu<sup>+</sup> transient species mediate the reconstruction of copper electrocatalysts for CO<sub>2</sub> reduction. *Nat. Catal.* **7**, 89 (2024).
26. Sun, Y. et al. The facile dissociation of carbon–oxygen bonds in CO<sub>2</sub> and CO on the surface of LaCoSiH<sub>x</sub> intermetallic compound. *Angew. Chem. Int. Ed.* **133**, 25742 (2021).
27. Sun, Y. et al. Water-induced structural evolution of LaTMSi ternary intermetallic electrides. *Chem. Mater.* **35**, 1972 (2023).
28. Gong, Y. et al. Ternary intermetallic LaCoSi as a catalyst for N<sub>2</sub> activation. *Nat. Catal.* **1**, 178 (2018).
29. Gong, Y. et al. Unique catalytic mechanism for Ru-loaded ternary intermetallic electrides for ammonia synthesis. *J. Am. Chem. Soc.* **144**, 8683 (2022).
30. Lu, Y. et al. Synthesis of rare-earth-based metallic electride nanoparticles and their catalytic applications to selective hydrogenation and ammonia synthesis. *ACS Catal.* **8**, 11054 (2018).
31. Hosono, H. & Kitano, M. Advances in materials and applications of inorganic electrides. *Chem. Rev.* **121**, 3121 (2021).
32. Yuan, X. et al. Crystal structure prediction approach to explore the iron carbide phases: novel crystal structures and unexpected magnetic properties. *J. Phys. Chem. C* **124**, 17244 (2020).
33. Ye, T. et al. Copper-based intermetallic electride catalyst for chemoselective hydrogenation reactions. *J. Am. Chem. Soc.* **139**, 17089 (2017).
34. Wu, H. et al. Selective and energy-efficient electrosynthesis of ethylene from CO<sub>2</sub> by tuning the valence of Cu catalysts through aryl diazonium functionalization. *Nat. Energy* **9**, 422 (2024).
35. Fu, W. et al. Photoinduced loading of electron-rich Cu single atoms by moderate coordination for hydrogen evolution. *Nat. Commun.* **13**, 5496 (2022).
36. Wan, B. et al. BaCu, a two-dimensional electride with Cu anions. *J. Am. Chem. Soc.* **146**, 17508 (2024).
37. Zhang, Z. et al. The most active Cu facet for low-temperature water gas shift reaction. *Nat. Commun.* **8**, 488 (2017).
38. Fan, L. et al. Proton sponge promotion of electrochemical CO<sub>2</sub> reduction to multi-carbon products. *Joule* **6**, 205 (2022).
39. Gao, W. et al. Experimental evidence of distinct sites for CO<sub>2</sub>-to-CO and CO conversion on Cu in the electrochemical CO<sub>2</sub> reduction reaction. *Nat. Catal.* **6**, 885 (2023).
40. Delmo, E. P. et al. In situ infrared spectroscopic evidence of enhanced electrochemical CO<sub>2</sub> reduction and C–C coupling on oxide-derived copper. *J. Am. Chem. Soc.* **146**, 1935 (2024).
41. Li, P. et al. Hydrogen bond network connectivity in the electric double layer dominates the kinetic pH effect in hydrogen electrocatalysis on Pt. *Nat. Catal.* **5**, 900 (2022).
42. Gomes, R. J. et al. Modulating water hydrogen bonding within a non-aqueous environment controls its reactivity in electrochemical transformations. *Nat. Catal.* **7**, 689 (2024).
43. Mi, Z., Wang, T., Xiao, L., Wang, G. & Zhuang, L. Catalytic peculiarity of alkali metal cation-free electrode/ polyelectrolyte interfaces toward CO<sub>2</sub> reduction. *J. Am. Chem. Soc.* **146**, 17377 (2024).
44. Zhu, Z. et al. Covalent organic framework ionomer steering the CO<sub>2</sub> electroreduction pathway on Cu at industrial-grade current density. *J. Am. Chem. Soc.* **146**, 1572 (2024).
45. Zhao, J. et al. Modulation of \*CH<sub>x</sub>O adsorption to facilitate electrocatalytic reduction of CO<sub>2</sub> to CH<sub>4</sub> over Cu-based catalysts. *J. Am. Chem. Soc.* **145**, 6622 (2023).
46. Blöchl, P. E. Projector augmented-wave method. *Phys. Rev. B* **50**, 17953 (1994).
47. Kresse, G. & Joubert, D. From ultrasoft pseudopotentials to the projector augmented-wave method. *Phys. Rev. B* **59**, 1758 (1999).
48. Perdew, J., Burke, K. & Ernzerhof, M. Generalized gradient approximation made simple. *Phys. Rev. Lett.* **77**, 3865 (1996).
49. Kresse, G. & Furthmüller, J. Efficient iterative schemes for ab initio total-energy calculations using a plane-wave basis set. *Phys. Rev. B* **54**, 11169 (1996).
50. Kresse, G. & Furthmüller, J. Efficiency of ab-initio total energy calculations for metals and semiconductors using a plane-wave basis set. *Comput. Mater. Sci.* **6**, 15 (1996).
51. Methfessel, M. & Paxton, A. T. High-precision sampling for Brillouin-zone integration in metals. *Phys. Rev. B* **40**, 3616 (1989).
52. Grimme, S., Antony, J., Ehrlich, S. & Krieg, H. A consistent and accurate ab initio parametrization of density functional dispersion correction (DFT-D) for the 94 elements H–Pu. *J. Chem. Phys.* **132**, 154104 (2010).
53. Monkhorst, H. J. & Pack, J. D. Special points for Brillouin-zone integrations. *Phys. Rev. B* **13**, 5188 (1976).
54. Nørskov, J. K. et al. Origin of the overpotential for oxygen reduction at a fuel-cell cathode. *J. Phys. Chem. B* **108**, 17886 (2004).
55. Rossmeisl, J. et al. Electrolysis of water on oxide surfaces. *J. Electroanal. Chem.* **607**, 83 (2007).
56. Wang, V. et al. Vaspkit: A user-friendly interface facilitating high-throughput computing and analysis using vasp code. *Comput. Phys. Commun.* **267**, 108033 (2021).
57. Henkelman, G., Uberuaga, B. P. & Jónsson, H. A climbing image nudged elastic band method for finding saddle points and minimum energy paths. *J. Chem. Phys.* **113**, 9901 (2000).
58. Akhade, S. A. et al. A simple method to approximate electrode potential-dependent activation energies using density functional theory. *Catal. Today* **288**, 63 (2017).
59. Dai, Y. et al. Manipulating local coordination of copper single atom catalyst enables efficient CO<sub>2</sub>-to-CH<sub>4</sub> conversion. *Nat. Commun.* **14**, 3382 (2023).

60. Tan, X. et al. Stabilizing copper by a reconstruction-resistant atomic Cu–O–Si interface for electrochemical CO<sub>2</sub> reduction. *J. Am. Chem. Soc.* **145**, 8656 (2023).
61. Zhou, X. et al. R Stabilizing Cu<sup>2+</sup> ions by solid solutions to promote CO<sub>2</sub> electroreduction to methane. *J. Am. Chem. Soc.* **144**, 2079 (2022).
62. Chen, S. et al. Highly selective carbon dioxide electroreduction on structure-evolved copper perovskite oxide toward methane production. *ACS Catal.* **10**, 4640 (2020).
63. Chen, S. et al. MOF encapsulating N-heterocyclic carbene-ligated copper single-atom site catalyst towards efficient methane electrosynthesis. *Angew. Chem. Int. Ed.* **134**, e202114450 (2022).
64. Han, Z. et al. Steering surface reconstruction of copper with electrolyte additives for CO<sub>2</sub> electroreduction. *Nat. Commun.* **13**, 3158 (2022).
65. Liu, J. et al. Switching between C<sub>2</sub><sup>+</sup> products and CH<sub>4</sub> in CO<sub>2</sub> electrolysis by tuning the composition and structure of rare-earth/copper catalysts. *J. Am. Chem. Soc.* **145**, 23037 (2023).
66. Wang, R. et al. Partial coordination-perturbed Bi-copper sites for selective electroreduction of CO<sub>2</sub> to hydrocarbons. *Angew. Chem. Int. Ed.* **60**, 19829 (2021).
67. Liu, K. et al. Unraveling and tuning the linear correlation between CH<sub>4</sub> and C<sub>2</sub> production rates in CO<sub>2</sub> electroreduction. *Sci. Bull.* **67**, 1042 (2022).
68. Xia, C. et al. Highly selective electrocatalytic CO<sub>2</sub> conversion to tailored products through precise regulation of hydrogenation and C–C coupling. *J. Am. Chem. Soc.* **146**, 20530 (2024).
69. Chen, S. et al. Lewis acid site-promoted single-atomic Cu catalyzes electrochemical CO<sub>2</sub> methanation. *Nano Lett.* **21**, 7325 (2021).
70. Zhang, L. et al. Enhanced cuprophilic interactions in crystalline catalysts facilitate the highly selective electroreduction of CO<sub>2</sub> to CH<sub>4</sub>. *J. Am. Chem. Soc.* **143**, 3808 (2021).
71. Jiang, Y. et al. Pushing the performance limit of Cu/CeO<sub>2</sub> Catalyst in CO<sub>2</sub> electroreduction: A cluster model study for loading single atoms. *ACS Nano* **17**, 2620 (2023).
72. Zhang, Y. et al. Coordination environment dependent selectivity of single-site-Cu enriched crystalline porous catalysts in CO<sub>2</sub> reduction to CH<sub>4</sub>. *Nat. Commun.* **12**, 6390 (2021).
73. Pan, F. et al. N and OH-immobilized Cu<sub>3</sub> clusters in situ reconstructed from single-metal sites for efficient CO<sub>2</sub> electromethanation in bicontinuous mesochannels. *J. Am. Chem. Soc.* **146**, 1423 (2024).
74. Xiong, L. et al. Geometric modulation of local CO Flux in Ag@Cu<sub>2</sub>O nanoreactors for steering the CO<sub>2</sub>RR pathway toward high-efficacy methane production. *Adv. Mater.* **33**, 2101741 (2021).
75. Zhang, Y. et al. Tailoring coordination microenvironment of Cu(I) in metal–organic frameworks for enhancing electroreduction of CO<sub>2</sub> to CH<sub>4</sub>. *Adv. Funct. Mater.* **32**, 2203677 (2022).
76. Jeon, H. S. et al. Selectivity control of Cu nanocrystals in a gas-fed flow cell through CO<sub>2</sub> pulsed electroreduction. *J. Am. Chem. Soc.* **143**, 7578 (2021).
77. Jiao, J. et al. Steering the reaction pathway of CO<sub>2</sub> electroreduction by tuning the coordination number of copper catalysts. *J. Am. Chem. Soc.* **146**, 15917 (2024).

## Acknowledgements

This research is financial supported by the Ministry of Science and Technology of China (Grant No. 2022YFA1604100[X.W.]), the National Science Fund for Distinguished Young Scholars of China (Grant No. 22225206[X.W.]), the CAS Project for Young Scientists in Basic Research (YSBR-005[X.W.]), the Key Research Program of Frontier Sciences CAS (ZDBS-LY-7007[X.W.]), the Major Research Plan of the National Natural Science Foundation of China (92045303[X.W.]), the Informatization Plan of Chinese Academy of Sciences (Grant No. CAS-WX2021SF0110[X.W.]),

the National Natural Science Foundation of China (Grant No. 22372188[X.W.]), the Ministry of Science and Technology of China (Grant No. 2022YFA1604100[F.W.]), the Innovation Foundation of the Institute of Coal Chemistry, Chinese Academy of Sciences (SCJC-HN-2023-14[F.W.]), and Synfuels China Co., Ltd. We gratefully acknowledge Y. J. Jiang, Y. L. Bai, and Z. G. Lv at Synfuels China Co., Ltd. for assistance in performing GC, H<sub>2</sub>O-TPSR, and XPS analysis, respectively. The authors also acknowledge H. C. Chen and W. Yin for assistance with the neutron powder diffraction experiments performed at the Multi-Physics Instrument (MPI) of the China Spallation Neutron Source (CSNS) in Dongguan, China; W. T. Zheng (State Key Laboratory of Coal Conversion, CAS) and the staff of the BL17B and BL20U1 beamlines in Shanghai Advanced Research Institute, Chinese Academy of Sciences, for their technical support in XAFS data collection and analysis. X. C. Liu (State Key Laboratory of Coal Conversion, CAS) for help with theoretical calculations.

## Author contributions

L.Z. designed and performed the experiments, and wrote the manuscript. H.M. performed the DFT calculations. Y.S. provided guidance on catalyst preparation and performed the XAS tests. Y.Z. assisted in the analysis of the in-situ IR data. H.D. and Y.W. provided help with the testing of the CO<sub>2</sub>RR. M.L. F.W. and X.W. conceived the idea and supervised the project. All authors discussed, commented on, and revised the manuscript.

## Competing interests

The authors declare no competing interests.

## Additional information

**Supplementary information** The online version contains supplementary material available at <https://doi.org/10.1038/s41467-025-60353-9>.

**Correspondence** and requests for materials should be addressed to Fei Wang, Xiao-Dong Wen or Mingchuan Luo.

**Peer review information** *Nature Communications* thanks Yuan-Biao Huang, Min Kuang, Adithya Polasa, and the other, anonymous, reviewer(s) for their contribution to the peer review of this work. A peer review file is available.

**Reprints and permissions information** is available at <http://www.nature.com/reprints>

**Publisher's note** Springer Nature remains neutral with regard to jurisdictional claims in published maps and institutional affiliations.

**Open Access** This article is licensed under a Creative Commons Attribution-NonCommercial-NoDerivatives 4.0 International License, which permits any non-commercial use, sharing, distribution and reproduction in any medium or format, as long as you give appropriate credit to the original author(s) and the source, provide a link to the Creative Commons licence, and indicate if you modified the licensed material. You do not have permission under this licence to share adapted material derived from this article or parts of it. The images or other third party material in this article are included in the article's Creative Commons licence, unless indicated otherwise in a credit line to the material. If material is not included in the article's Creative Commons licence and your intended use is not permitted by statutory regulation or exceeds the permitted use, you will need to obtain permission directly from the copyright holder. To view a copy of this licence, visit <http://creativecommons.org/licenses/by-nc-nd/4.0/>.

© The Author(s) 2025